Supplementary Information

Fast-Response Biomimetic Phototropic Material Built by Coordination-Assisted Photothermal Domino Strategy

Zhikai Tu,[a] Jin Wang,[c] Weifeng Liu,*[a] Zhijun Chen,[d] Jinhao Huang,[a] Jinxing Li,[a] Hongming Lou[a] and Xueqing Qiu*[b]

[a] School of Chemistry and Chemical Engineering, Guangdong Provincial Key Lab of Green Chemical Product Technology, State Key Laboratory of Pulp and Paper Engineering, South China University of Technology, Guangzhou 510640, P. R. China.
E-mail: weifengliu@scut.edu.cn
[b] School of Chemical Engineering and Light Industry, Guangdong University of Technology, Guangzhou 510006, P. R. China.
E-mail: cexqqiu@scut.edu.cn
[c] The National Engineering Research Center of Novel Equipment for Polymer Processing, School of Mechanical & Automotive Engineering, South China University of Technology, Guangzhou 510640, P. R. China.
[d] Engineering Research Center of Advanced Wooden Materials and Key Laboratory of Bio-based Material Science & Technology Ministry of Education, Northeast Forestry University, Harbin 150040, P. R. China.

Experimental Section

Materials: EPDM 3745P (ethylene 70 wt%, propylene 29.5 wt%, ethylidene norbornene 0.5 wt%) with antioxidant 1010 was obtained from Dow Chemical. Industrial kraft lignin was provided by Shanghai Changfa New Material Co. with the purity of 95%, weight average molecular weight of 3000 Da and the molecular weight distribution index of 3.2. The total hydroxyl content was about 3.94 mmol/g. The purified kraft lignin powder cost about 3000~3500 RMB per ton, which is much cheaper than carbon black, e.g. carbon black N330 that commonly used in China rubber industry costs more than 9000 RMB per ton. Zinc dimethacrylate (ZDMA) was purchased from Sigma-Aldrich. Dicumyl peroxide (DCP) was received from Shanghai Aladdin Biochemical Technology Co., Ltd.

Sample preparation: Firstly, lignin (6 phr) and a certain amount of ZDMA was added to a commercially available zirconia ceramics reactor along with zirconia ball bearings (30 g), followed by the addition of ethanol (10 mL). Then the reactor was placed in a high-speed vibrating ball miller (300 rounds per min) for one hour of forward and reverse rotation, and the final lignin/ZDMA coordination compound was obtained after dried in a vacuum oven at 50 °C for 24 h. The sample was named as LxZy coordination compound, with "L" for lignin, "Z" for ZDMA. Secondly, lignin/ZDMA coordination compound was mixed with EPDM (100 phr) at 50 rpm and 110 °C for 10 mins in an internal mixer (Guangdong Lina Co., Ltd., Dongguan, China). Next, DCP was added and mixed for another 5 mins, followed by hot-pressing at 130 °C for 20 mins. All the composite materials were cut into the needed shape (dumbbell or ribbon) for further study. The sample was named as P100LxZy, with "P" standing for EPDM, "L" for lignin, "Z" for ZDMA, and the numbers x and y for the parts per hundred of EPDM (100 phr). Finally, the vulcanized elastomer was repetitively stretched for 250 times at a fixed strain by electronic universal testing machine (MTS, China) to get the artificial phototropism materials P100LxZy@m%. "@" representing for mechanical training, the number m for the mechanical training strain. For instance, P100L6Z15@800% means EPDM 100 phr, lignin 6 phr, ZDMA 15 phr, and the fixed 600% training strain. P100L6Z15 means the sample was not submitted for mechanical training. All the samples after mechanical training were rested for half an hour prior to use.

Characterizations: Infrared (IR) spectra of the lignin/ZDMA coordination compound was obtained on a Thermo Nicolet FTIR spectrometer (US) with the scanning range from 4000 to 400 cm^{-1}. The samples were measured by the KBr tablet method. Infrared spectra of the

lignin/ZDMA/EPDM composites were studied by Bruker Vertex 70 FTIR spectrometer (Bruker, Germany) at the attenuated total reflection (ATR) mode.

Ultraviolet-visible-near-infrared spectra (UV-Vis-NIR) was collected on a Lamdba 950 UV-Vis-NIR spectrometer (Platinum Elmer Instruments Co., Ltd., USA) at attenuated total reflection (ATR) mode for testing the light absorption of lignin at 200-1250 nm.

Electron paramagnetic resonance (EPR) testing of precursor was performed on Bruker EPR EMX_Plus. The spectrometer was operated at X band (9.83 GHz), sweep width of 100.0 G, and sweep time of 30 s, and the spectra were obtained with a 100-kHz field modulation at 6.325 mW power. Xenon lamp was chosen as irradiation light source. All the free radical concentrations were calculated according to the volume of lignin.

The scanning electron microscopy (SEM) was conducted on a Hitachi UHR FE-SEM SU8220 instrument (Hitachi, Tokyo, Japan) with an accelerating voltage of 5 kV, and the samples were sputtered with a thin gold film before test to enhance the conductivity.

Mechanical training and tensile tests were carried out on a CMT electronic universal testing machine (MTS, China) with the speed of 200 mm/min at room temperature.

Dynamic mechanical analyzer (DMA 850, TA instrument, USA) was used to measure the actuation stress and actuation strain of the samples. As for P100L6Z15 without mechanical training, the residual strain was preset at 55 ºC, and then was cooling at 0 ºC for stabilizing the residual strain (same as P100L6Z15@600%). And for L6Z15@600%, the sample was rested for half hour after mechanical training. In the isoforce tests, constant stress (1.2 MPa) was first applied to the sample, the sample was cooled to -30 °C, and then the actuation strain was recorded along with the temperature varied from -30 °C to 55 °C at a rate of 3.0 °C/min. The actuation strain was defined as (L−L0)/L0, where L is the real-time length of the sample measured at any temperature and L0 is the initial length before testing. In the isostrain experiments, constant strain was first fixed at 0.01%, the sample was cooled to -30 °C, and then the actuation stress was recorded along with the temperature ranged from -30 °C to 55 °C at a rate of 3.0 °C/min.

The specific heat capacity and the melting point were determined on a DSC 2500 calorimeter (TA instrument, USA). The specific heat capacity test procedure was as follows: The temperature was first set to 25 °C, kept constant for 5 min, then raised to 250 °C at 5 °C/min, and kept constant temperature for 5 min. The specific heat capacity was collected from the temperature range of 25~250 °C; The melting point was tested as follows: The temperature was first increased to 180 °C at a heating rate of 10 °C/min, and was kept constant for 3 min to eliminate the thermal history. Then the temperature was reduced to -85

°C at a rate of 10 °C/min, and was kept constant for 3 min. Finally the temperature was increased to 180 °C at a rate of 10 °C/min. The melting temperature (T_m) was obtained from the second heating process.

For the photothermal test, a 808 nm semiconductor laser emitter (Lasever Inc., China) was used as the light source, and an infrared camera (FLIR Systems, Inc., USA) was used as the temperature detection equipment. A xenon lamp (Beijing Perfectlight Technology Co., Ltd) was also used to monitor the solar light. The power density (W/cm^2) refers to the light intensity irradiated on the sample per unit area (cm^{-2}), which was adjusted by the distance between light source and sample and was tested by optical power meter (PL-MW 2000, Beijing Perfectlight Technology Co., Ltd).

In the light-triggered actuation test, 20 mg sample P100L6Z15@600% was attached to a 205 g load, and heated and cooled down, the load were lifted up and down, a reversible strain were observed and recorded. The temperature inside the sample was detected by the infrared camera (FLIR T530, 30 mK thermal sensitivity).

The thermo-oxidative aging test was carried out in a NR8851 thermo-oxidative age-circulating oven (Nayu Instruments Co., Ltd., China) at 100 °C for 3 days. And ultraviolet (UV) aging was performed in WT-uvA Ultraviolet age-circulating oven (Wangjia Instruments Co., Ltd., China) at 40 °C for 6 days. Then, mechanical properties of samples before and after the aging test were compared.

The non-contact full field deformation measurement of the sample was achieved by the 2D digital image correlation (DIC) techniques. Before the measurement, the side of the sample P100L6Z15@600% that was parallel with the incident direction was coated with a thin layer of white paint and then sprayed with plenty of black dots. A camera for capturing the deformation process of the sample was set on the painted side of the sample; the view direction of the camera was set to be perpendicular with the painted side. The camera would take one picture every second in the light-tracking course. The displacement information of the black dots is contained in these pictures. With the help of the GOM Correlate software, the strain distribution in the painted side could be calculated. In a fixed coordinate system (x, y), let axis y be the original length direction of the sample, the gradient distribution of the strain in the y direction was shown for characterizing the asymmetric deformation of the sample during the light-tracking course.

The data of characterization

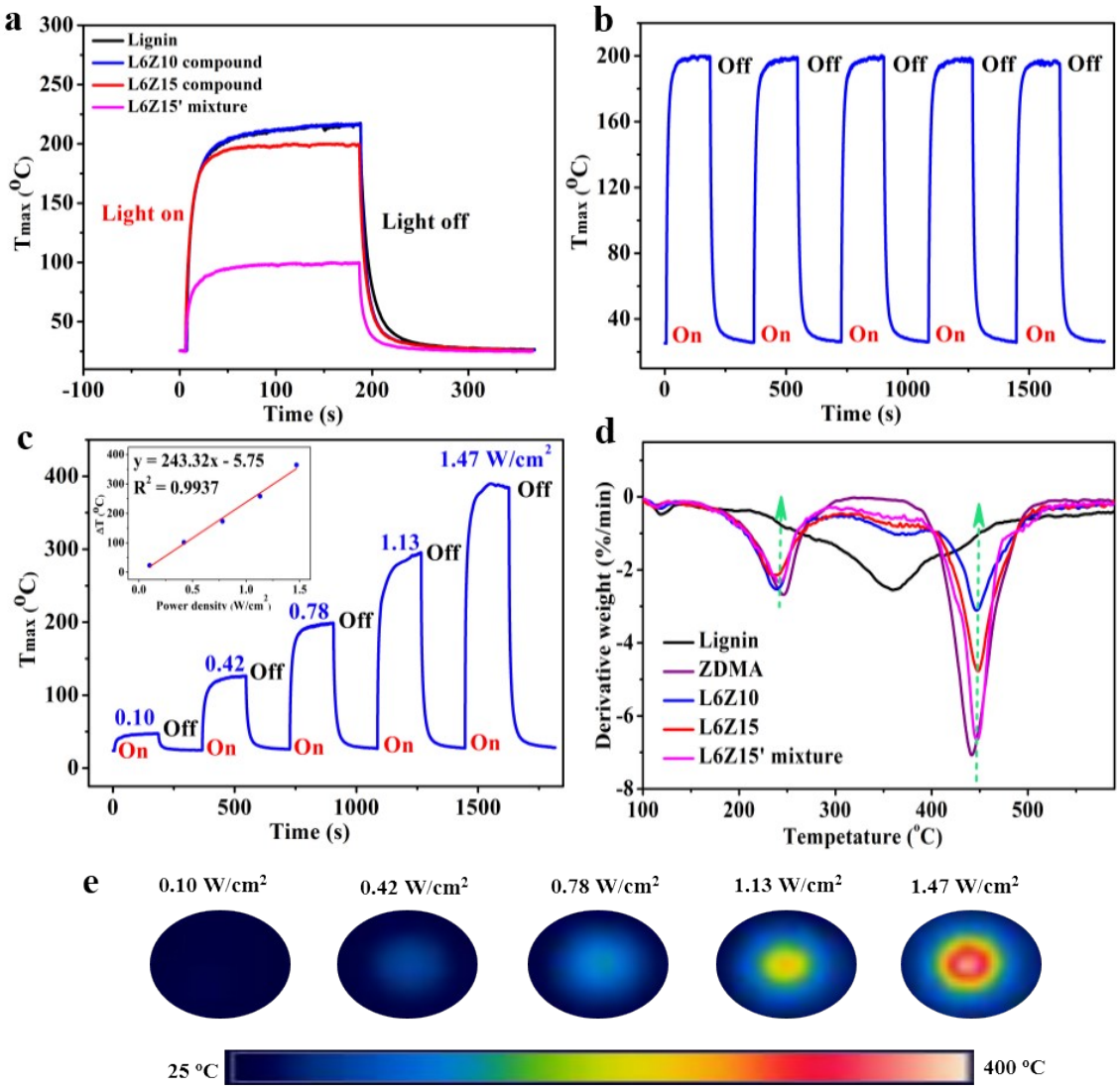

Fig. S1. Photothermal performance for coordination compounds under the NIR irradiation. a The surface maximum temperature variation for lignin, L6Z10 compound, L6Z15 compound and L6Z15' mixture under the illumination of 808 nm NIR laser with a power density of 0.78 W/cm^2. **b** The photostability of L6Z15 compound through alternative heating and cooling (5 cycles) by on-off 808 nm laser at 0.78·W/cm^2. **c** The surface maximum temperature variation for L6Z15 compound under the different light power densities (W/cm^2) of 808 nm NIR laser; Inset: the maximum temperature increment ΔT of L6Z15 compound versus the light power density. **d** The differential thermal gravity curves of for lignin, ZDMA, L6Z10 compound, L6Z15 compound and L6Z15' mixture. **e** Infrared thermal images of L6Z15 compound under the NIR irradiation (808 nm) with different power densities.

As shown in Fig. S1a, the maximum temperature (T_{max}) of L6Z15 compound rapidly increased from ambient temperature to 180 °C within 20 seconds and then gradually stabilized at 199 °C under the irradiation of NIR laser of 0.78 W/cm^2, confirming excellent

photothermal conversion of L6Z15 compound. When the light was turned off, the T_{max} of L6Z15 compound returned to room temperature quickly in 180 seconds. And this process could be stably repeated through alternative light-on heating and light-off cooling, demonstrating good photothermal stability of L6Z15 compound (Fig. S1b). Further investigation revealed that the T_{max} of L6Z15 compound was determined by the light power density (Fig. S1c, e), and the corresponding maximum temperature increment (ΔT) increased linearly from 23 °C (0.10 W/cm^2) to 365 °C (1.47 W/cm^2), which meant that the T_{max} of lignin compound could be precisely regulated by the light power density. Other lignin/ZDMA compounds also exhibited good photothermal conversion capacity. And the coordination effect in L6Z15 compound was also beneficial to increase the thermal stability (Fig. S1d).

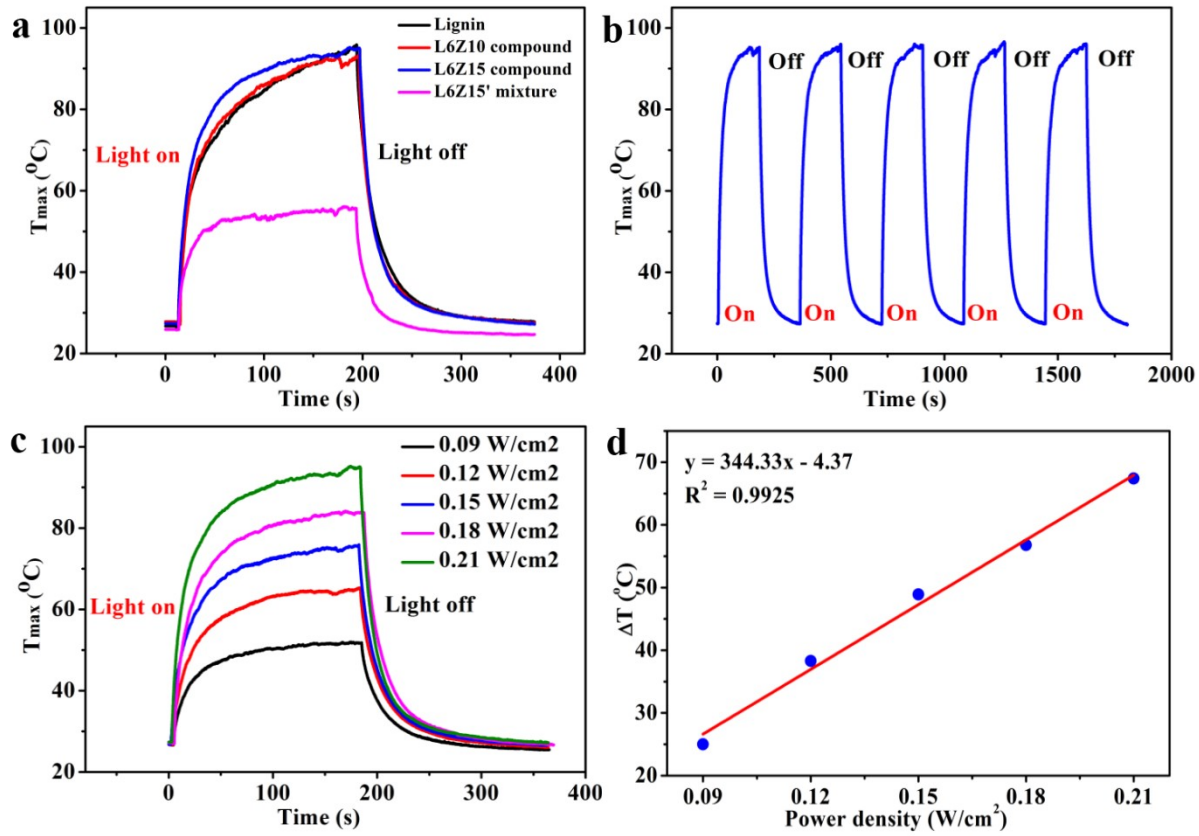

Fig. S2. Photothermal performance for coordination compounds under the broad-spectrum sunlight irradiation. a The surface maximum temperature variation for lignin, L6Z10 compound, L6Z15 compound and L6Z15' mixture under the illumination of the xenon lamp with a power density of 0.21 W/cm^2. **b** The photostability measurement of L6Z15 through alternative heating and cooling (5 cycles) by on-off xenon lamp at 0.21 W/cm^2; **c** The surface maximum temperature variation for L6Z15 under the different light power densities (W/cm^2) of xenon lamp. **d** The maximum temperature increment ΔT of L6Z15 compound versus the light power density.

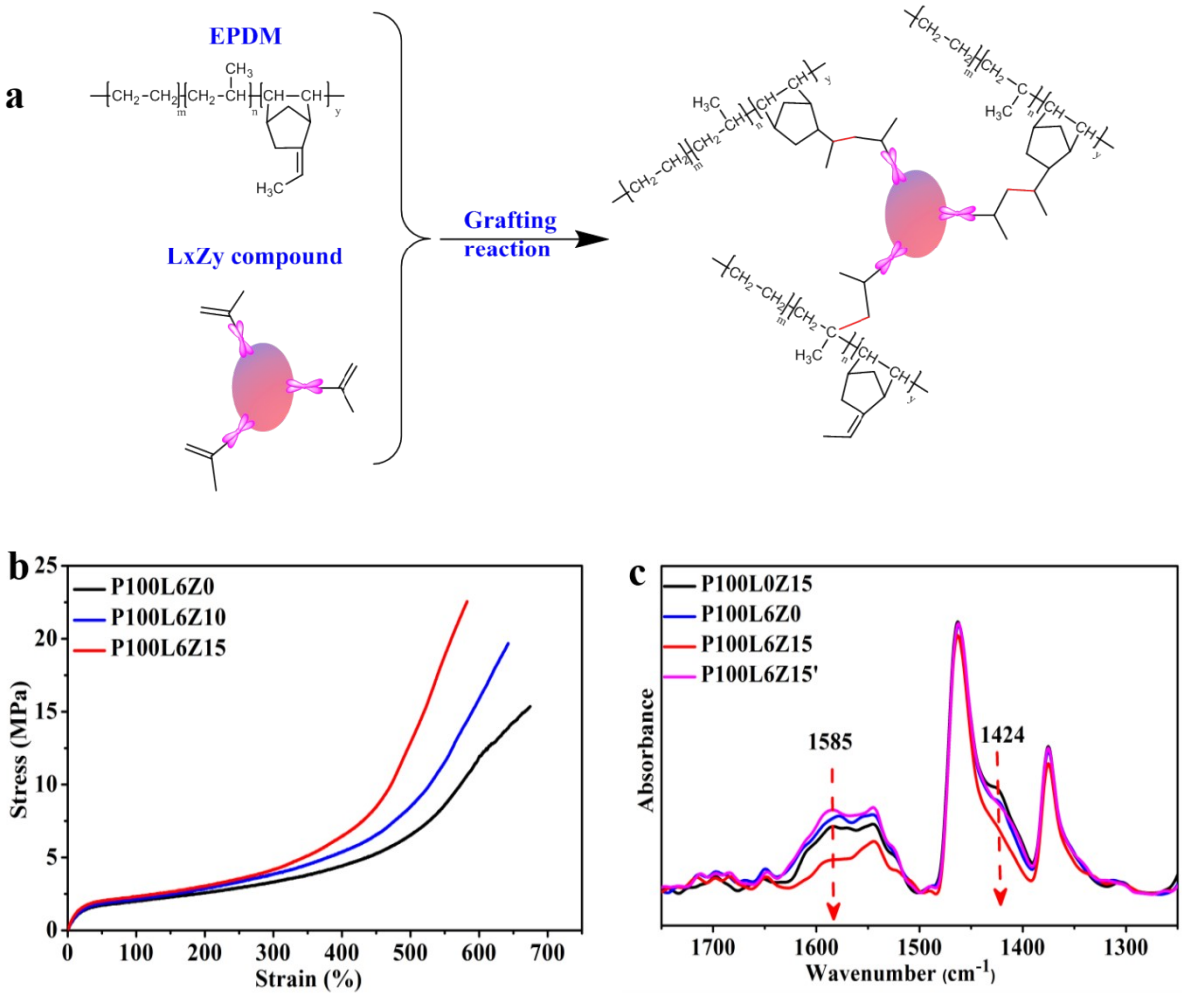

Fig. S3. The formation of interfacial coordination bonds. **a** The reaction mechanism between EPDM and LxZy compound; **b** The engineering stress-strain curves of elastomer composites with different coordination compounds. **c** The UV-Vis-NIR spectra for composites P100L0Z15 without lignin, P100L6Z0 without ZDMA, P100L6Z10 and P100L6Z15.

As shown in Supplementary Fig. 3b, the tensile strength of composites increased with the ZDMA content, due to the enhanced interfacial interaction between lignin and EPDM matrix by the coordination bonds. As shown in Fig. S3c, the peaks at 1544 cm^{-1} and 1424 cm^{-1} were assigned to symmetrical and anti-symmetrical vibrations of COO-[1] For P100L6Z15 with ball milling, both of these peaks had showed substantial decrease in intensity compared with P100L6Z0 and P100L0Z15, consistent with the result at Fig. 2a, confirming the coordination bonds were constructed in P100L6Z15. However, no variation was observed in these peaks for P100L0Z15' without ball milling, and its FTIR spectra curves were close to the sample P100L6Z0 without ZDMA, indicating ball mill is an efficient method for constructing coordination bonds.

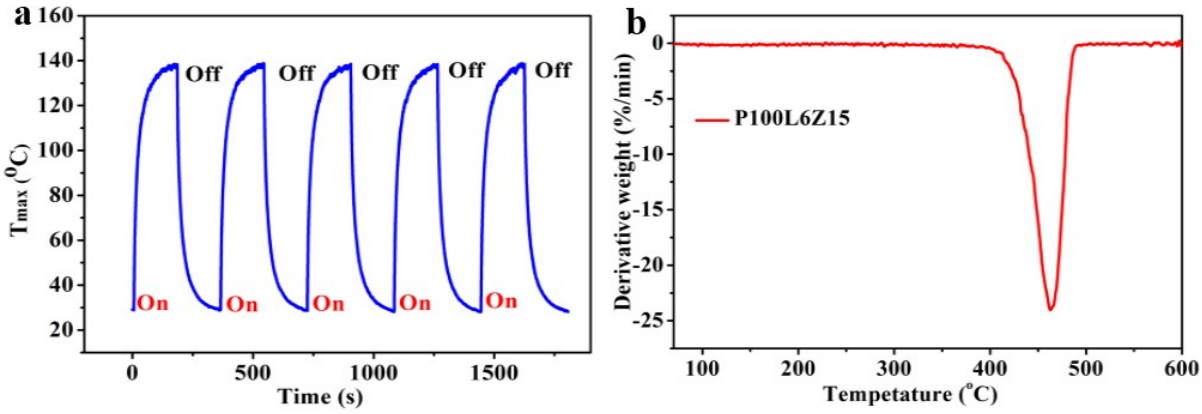

Fig. S4. Photothermal stability and thermal stability. a The photostability measurement of P100L6Z15 through alternative heating and cooling (5 cycles) by on-off 808 nm NIR laser at 0.78 W/cm^2. **b** The differential thermal gravity curve P100L6Z15.

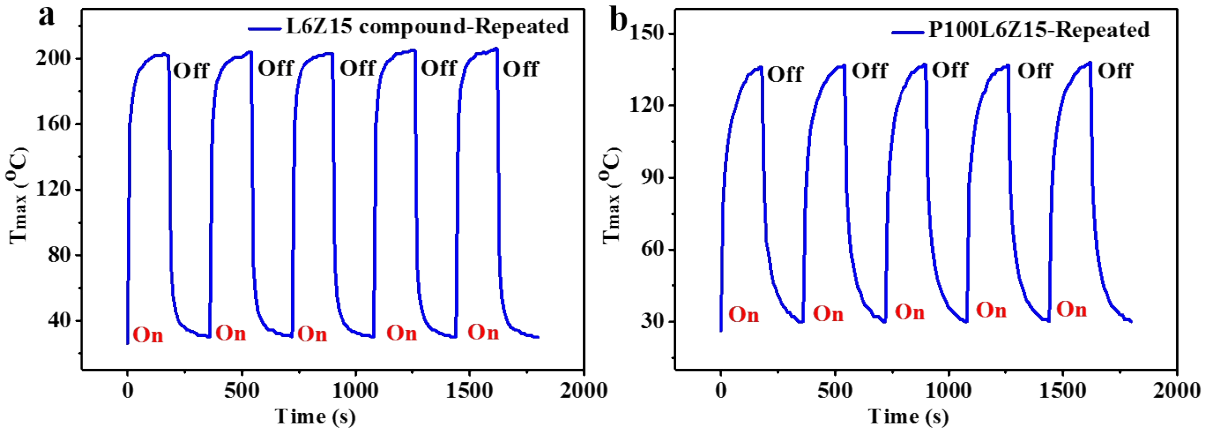

Fig. S5. Experimental repeatability. The repeated photothermal test for **a)** L6Z15 compound and **b)** P100L6Z15 composite after 9 mouths of storage.

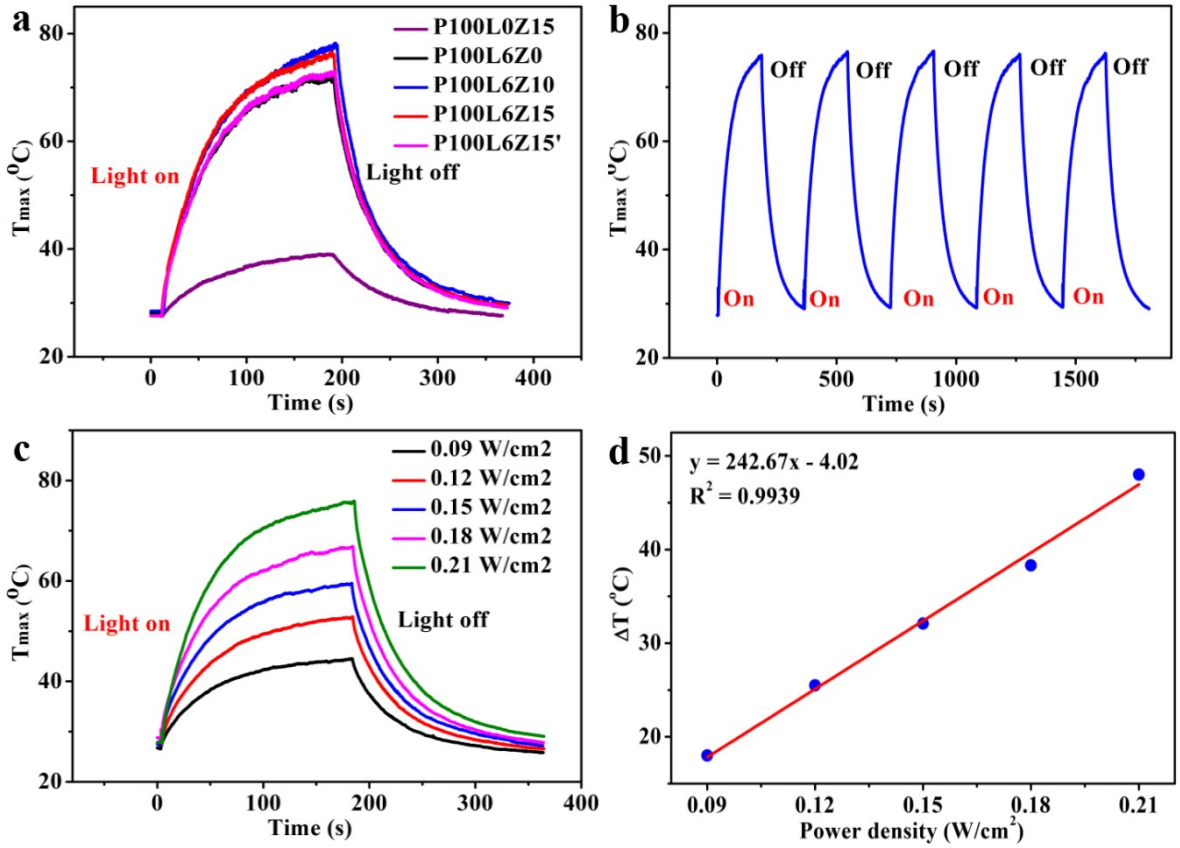

Fig. S6. Photothermal performance for composites under the broad-spectrum sunlight irradiation. a The surface maximum temperature variation for composites P100L0Z15 without lignin, P100L6Z0 without ZDMA, P100L6Z15 and P100L6Z15' (directly compounded without ball milling) under the illumination of xenon lamp with a power density of 0.21 W/cm^2. **b** The photostability measurement of P100L6Z15 through alternative heating and cooling (5 cycles) by on-off xenon lamp at 0.21 W/cm^2. **c** The surface maximum temperature variation for P100L6Z15 composite under the different light power densities (W/cm^2) of xenon lamp. **d** The maximum temperature increment ΔT of P100L6Z15 composite versus the light power density.

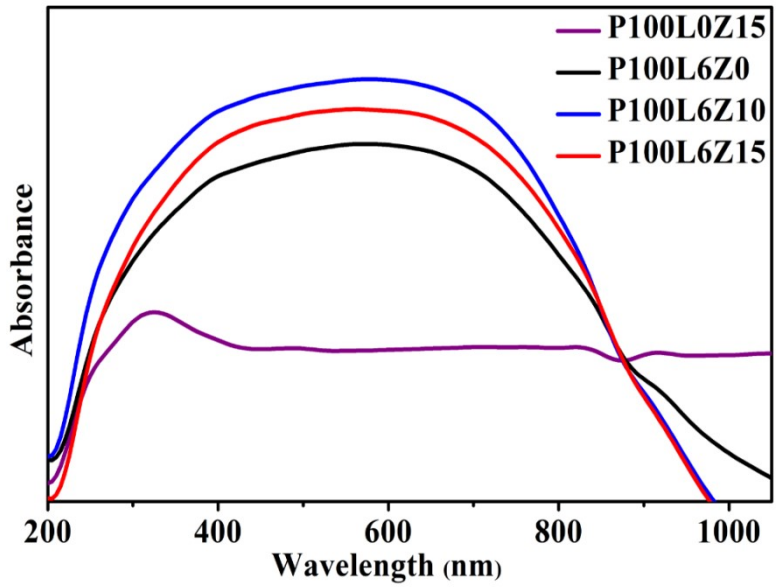

Fig. S7. Absorption property for composites. The normalized UV-Vis-NIR spectra for composites P100L0Z15 without lignin, P100L6Z0 without ZDMA, P100L6Z10 and P100L6Z15.

Though the ZDMA powder had no absorption at 530-860 nm wavelength and performed poor absorption at 280-530 nm (Fig. 3a), the samples P100L6Z15 and P100L6Z10 performed stronger UV-Vis-NIR light absorption than P100L6Z0 without ZDMA under the irradiation of 280-860 nm wavelength, demonstrating that the coordination effect in the elastomer composite was beneficial to catch more light energy and generate more heat energy, consistent with the performance of corresponding lignin coordination compounds (Fig. 3a).

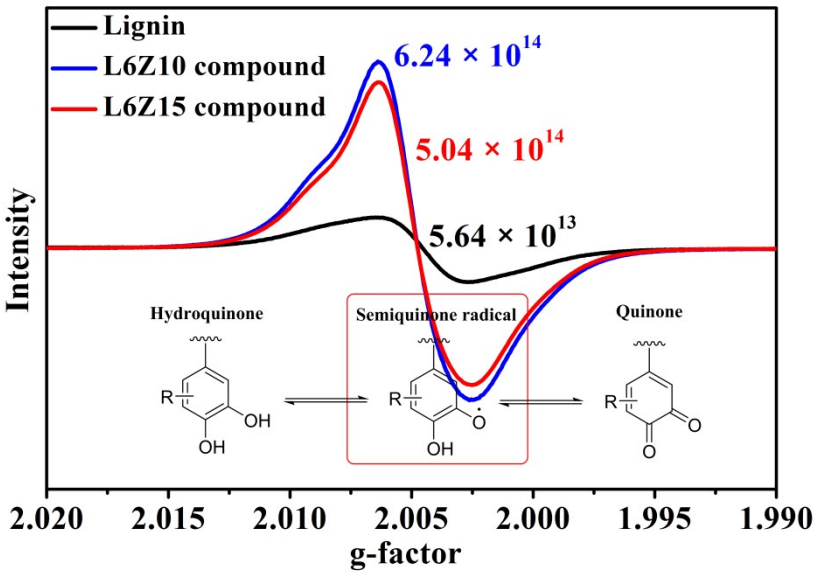

Fig. S8. EPR spectra for coordination compounds. The EPR spectra and the radical concentration of lignin and L6Z15 compound after the illumination of xenon lamp for 5 mins.

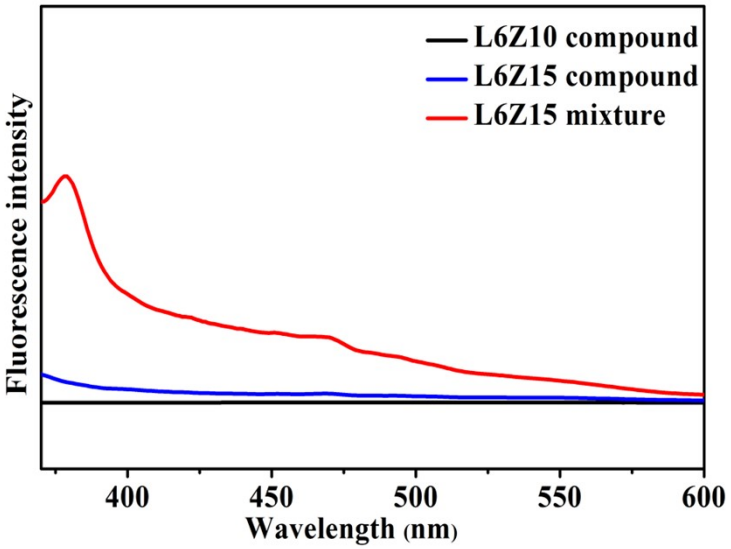

Fig. S9. Fluorescence spectra for coordination compounds. The fluorescence spectra for L6Z10 compound, L6Z15 compound and L6Z15 mixture under 350 nm excitation wavelength.

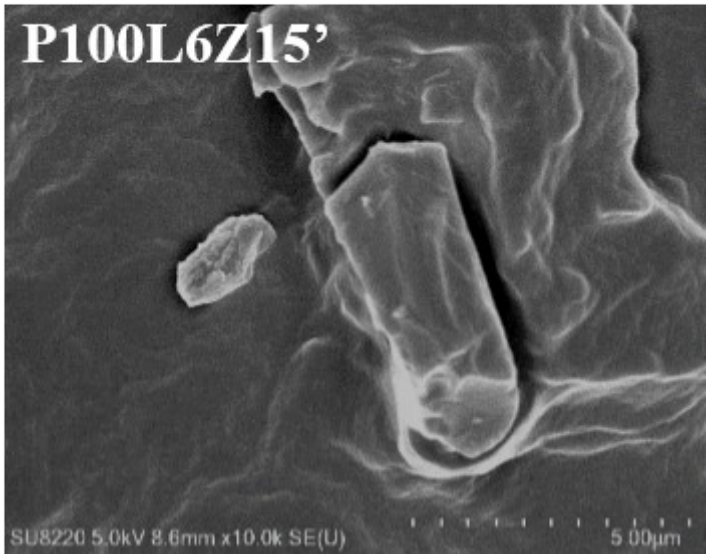

Fig. S10. Interfacial morphology for composites. The SEM image of the fracture surface for P100L6Z15' composites (directly compounded without ball milling).

The interfacial contact between lignin and polymer matrix was observed by SEM images shown in Fig. 2c and Fig. S10. For the directly blending sample P100L6Z0 without ZDMA and P100L6Z15' without formation of coordination bonds, the interface between the agglomerated lignin particles (>3 μm) and polymer matrix was obviously exfoliated, suggesting lower α and higher S_m (α↓ and S_m ↑), resulting in lower TCC coefficient (h_{eef} ↓), which restricted the heat conduction from thermal saturated lignin to low temperature EPDM. After introducing the interfacial coordination bonds for P100L6Z15, no obvious interface

exfoliation was observed between lignin (< 1 μm) and polymer matrix due to improved interfacial interaction, giving larger interfacial contact area (α ↑ and S_m ↓, h_{loc} ↑), which would result in higher TCC (h_{eef} ↑) and facilitate the heat transfer from lignin to EPDM matrix in time. The incorporation of interfacial coordination bonds was beneficial to increase the heat conduction between lignin and polymer matrix.

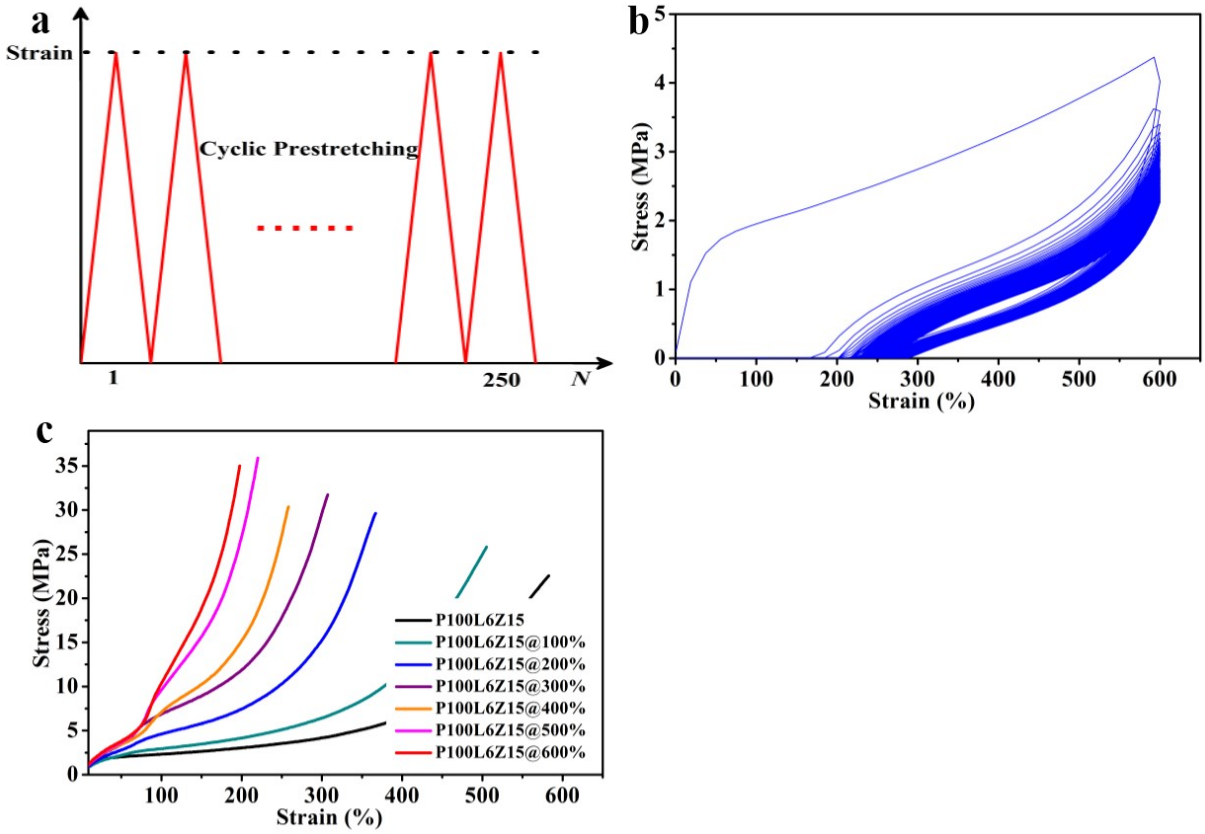

Fig. S11. Mechanical training process. **a** Illustration for the repeated pre-stretching of mechanical training process. **b** The loading-unloading curves of L40Z12@600% during mechanical training. **c** The engineering stress-strain curves of P100L6Z15 elastomer composites after mechanical training for 250 cycles at the stretching speed of 200 mm/min under different training strain.

The training process was conducted via repeated stretching and unloading and the corresponding stress–strain curves were illustrated in Fig. S11a&b. As the training strain increased from 100% to 600%, the tensile strength at failure increased gradually from 22.6 to 35.0 MPa (Fig. S11c). It was because that, the destruction and reconstruction process of the interfacial coordination bonds during the repetitive training not only contributed efficient energy dissipation, but also promoted the strain-induced crystallization of rubber chain segments, thus endowing the material with strong self-strengthening by mechanical training and strain-adaptive stiffening performance.

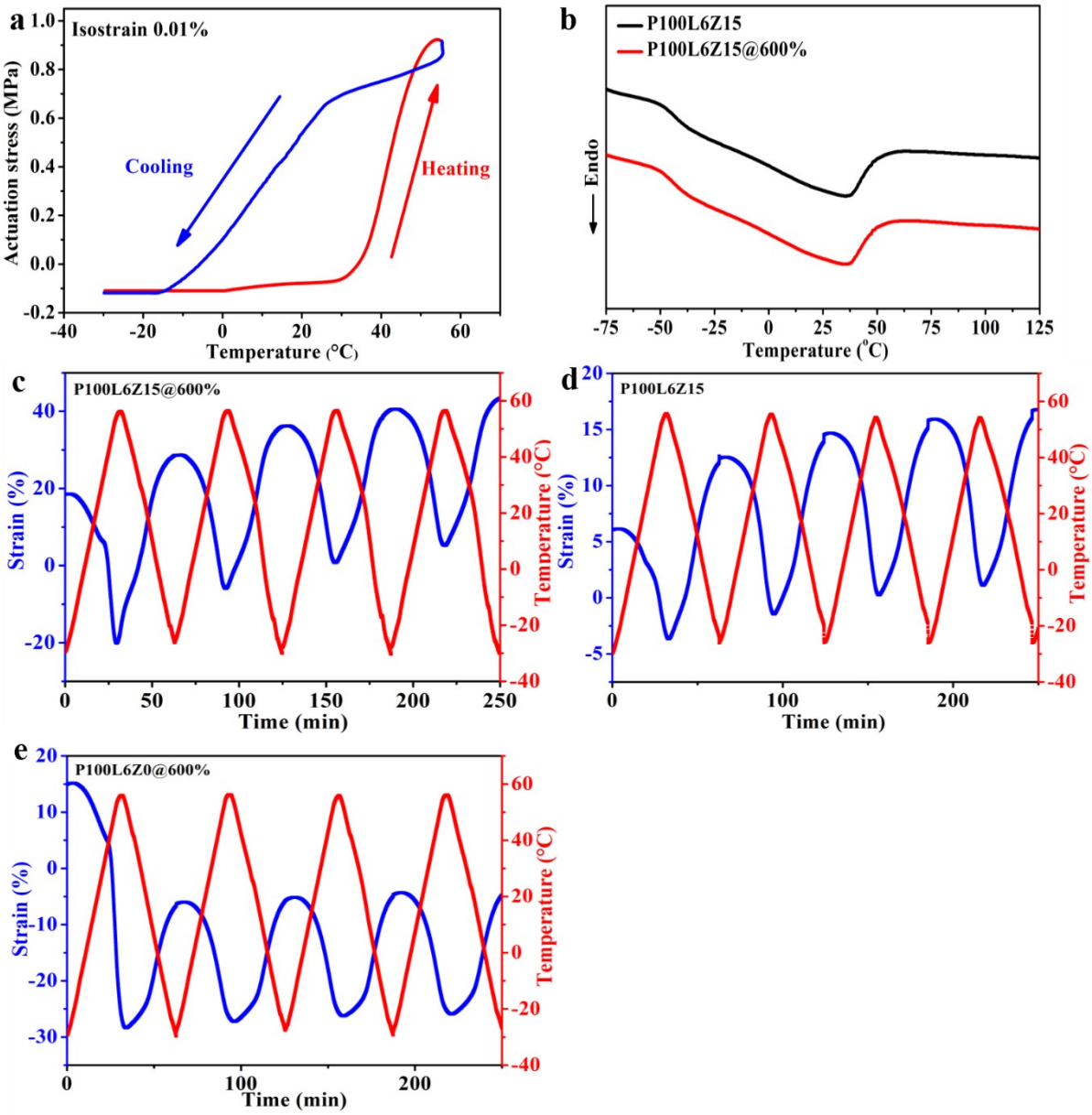

Fig. S12. Actuation perfoamance. a Stress variation in isostrain mode of P100L6Z15@600% plotted against temperature. **b** DSC crystallization curves of P100L6Z15 without mechanical training and P100L6Z15@600%. Stress variation and the corresponding temperature in iso-strain mode for **c** P100L6Z15@600%, **d** P100L6Z15 without mechanical training and **e** P100L6Z0@600% without ZDMA plotted against time.

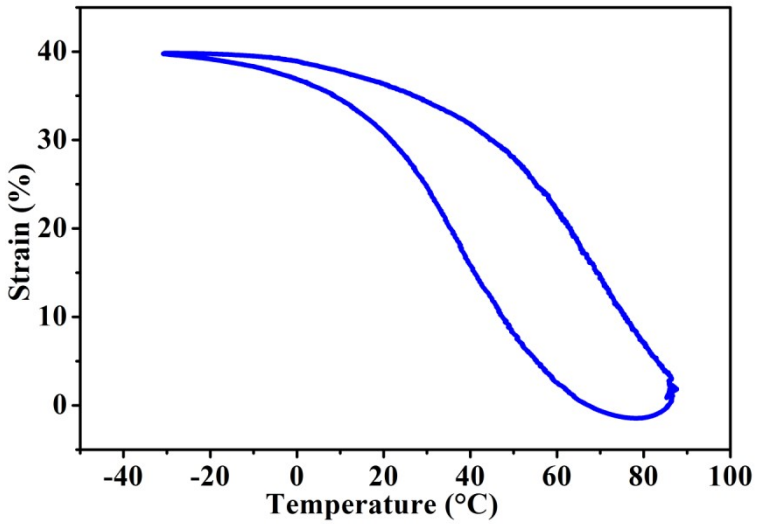

Fig. S13. Response temperature window for P100L6Z15@600%' with higher crosslinking density. Strain variation in iso-force mode for sample P100L6Z15@600% with higher crosslinking density plotted against temperature.

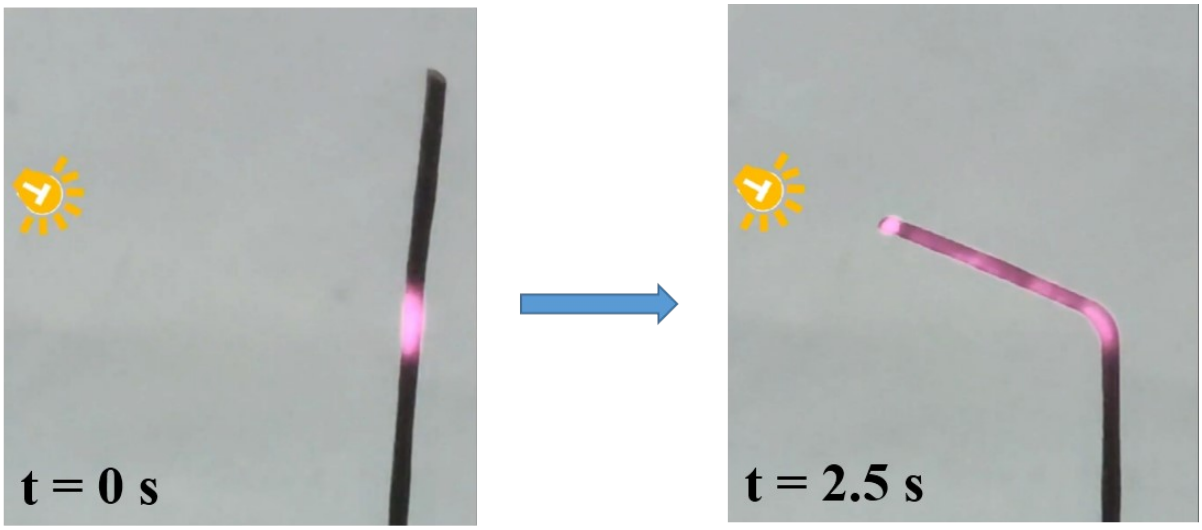

Fig. S14. Light-tracking performance. The light-tracking performance for P100L6Z15@600% under the illumination of NIR with a power density of 1.77 W/cm^2.

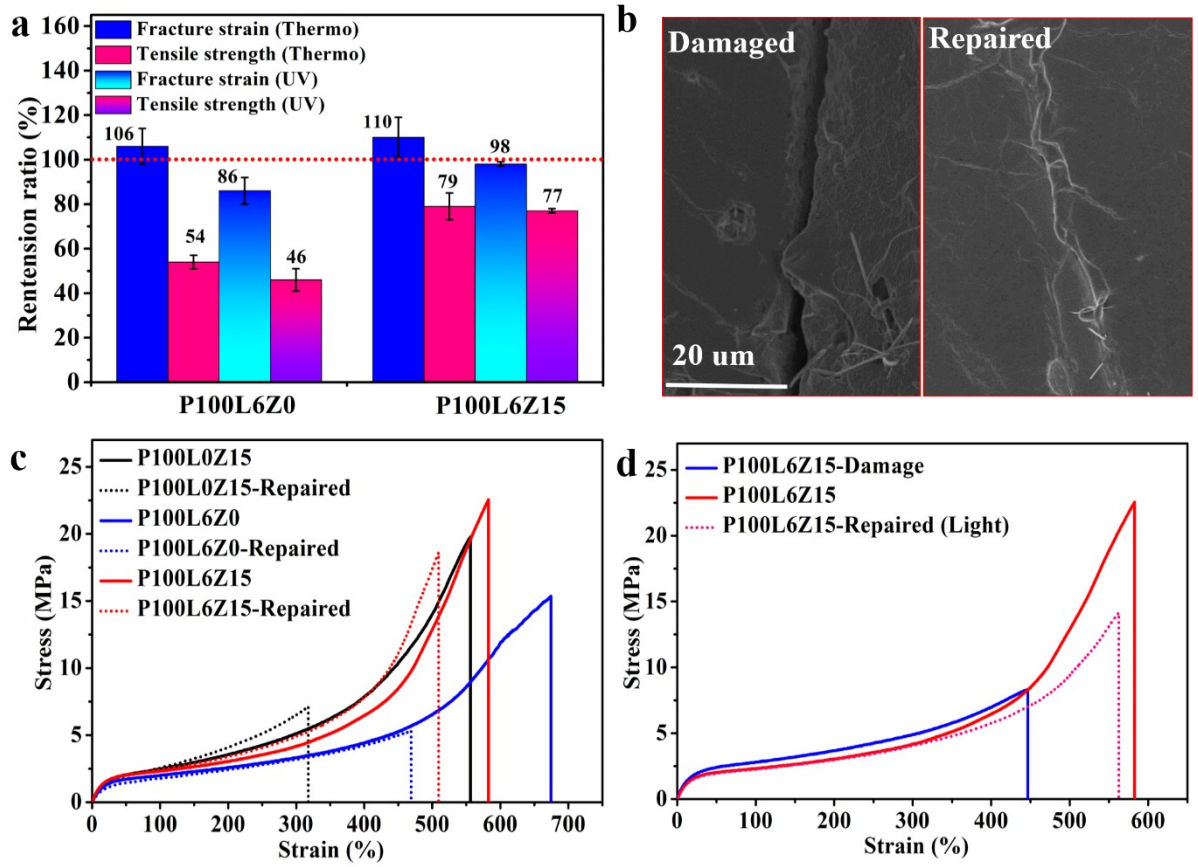

Fig. S15. Aging and self-repairing performance. a Retention ratio of mechanical properties of P100L6Z15, P100L6Z0 and P100L0Z15 composites after thermo-oxidative aging and ultraviolet (UV) aging. **b** SEM images of the damage surface before and after thermo repairing. **c** Stress–strain curves of original and thermo repaired sample (P100L6Z15, P100L6Z0 and P100L0Z15) repaired by 130 °C after 3h. **d** Stress–strain curves of original, damage and light healed sample for P100L6Z15.

Ageing resistance is a necessary property for artificial phototropism material to prevent damages from the sunlight. The effects of lignin and Zn^{2+}-based coordination bonds on the aging performance including thermo-oxidative aging and ultraviolet (UV) aging were investigated. The changes in the mechanical properties before and after aging test are shown in Fig. S15a. As for P100L6Z0 without ZDMA, the thermo-oxidative aging process, only 54% tensile strength was remained through thermo-oxidative aging process. After the UV aging process, the fracture strain was slightly decreased, but the retention ratio of tensile strength significantly decreased to 46%. This was because large number of free radicals was generated during aging process, which can attack on polymer main chains, leading to defects for the cross-linking network of P100L6Z0. When ZDMA was incorporated, after thermo-oxidative aging process, the retention ratio of tensile strength increased from 54% for P100L6Z0 to 79% for P100L6Z15, and for UV aging test, the retention ratio of tensile strength increased from

46% for P100L6Z0 to 77% for P100L6Z15, demonstrating the coordination bonds could enhance the ageing resistance. The reason could be that, the participation for coordination bonds could increase the concentration of free radicals in lignin (Fig. 3c), which can react with free radicals generated during aging process, terminating the chain reaction and maintaining the integrity of the cross-linking network of P100L6Z15.

The material has excellent ageing resistance that could delay the damage process from the sunlight, but mechanical damage is inevitable in the process of long-term utilization, thus the self-repairing ability is also necessary. Due to the dynamic destruction and reconstruction characteristic, the coordination bonds could not only strengthen the mechanical property during stretching, but also enhance the self-repairing property. To visually illustrate the self-repairing behavior, the surface morphologies of cut and repaired samples were determined via SEM. It can be seen in Fig. S15b that obvious crack was presented on the damage sample P100L6Z15, and the crack disappeared after repairing. In order to further quantitatively study on the self-repair performance under thermal stimulation, the mechanical performance was tested after damage and repairing. As shown in Fig. S15c, through repairing of 3h, the tensile strength and fracture strain of P100L6Z15 sample can be recovered to 84% and 87% of the original sample. But for sample P100L0Z15 without lignin and P100L6Z0 without ZDMA, the repairing efficiency of tensile strength and fracture strain were only 36%, 57% and 34%, 70% after heating 3h. Apparently, after heating, the coordination bonds could be reformed at the wound, followed by the fracture surface reconnected, thus endowing P100L6Z15 with excellent self-repairing performance.

As a precisely remote controllable tool without intervening surrounding environment, Near-Infrared (NIR) light could be used to achieving the regional repairing process through photothermal effect. The photothermal self-repairing performance of P100L6Z15 was also studied in Fig. S15d. Due to the materials superficial wounds are common in the daily usage, P100L6Z15 was scratched in the surface, and then heated at 130 ^{o}C under the irrigation of 808 nm light. The tensile strength and fracture strain were decreased to 37% and 77% of the original sample after surface damage. After 6h exposure irradiation, the tensile strength and fracture strain of the damaged material was repaired to 63% and 97% of the original sample, respectively. The excellent self-repairing performance through thermo/light stimulation is a good way to further improve the lifetime of artificial phototropism material and diminish carbon emissions from reproduction.

Explanation for DFT calculations and photothermal calculations

The DFT calculations were performed using Gaussian16.[2] For geometry optimization and frequency calculations, the PBE0[3,4] functional was adopted with the D3(BJ) empirical dispersion correction[5] and 6-311G(d) basis set.[6,7] The solvent effect of water was examined using the self-consistent reaction field (SCRF) method based on SMD model.[8]

The effective photothermal conversion was determined according to previous method.[9-11] General details are as follows:

Based on the total energy balance for this system:

$$\sum_i m_i C_{P,i} \frac{dT}{dt} = Q_s - Q_{loss}$$

(S1)

where m_i and $C_{p,i}$ are the mass and heat capacity of sample, respectively. Q_s is the photothermal heat energy input by irradiating NIR laser to samples, and Q_{loss} is thermal energy lost to the surroundings.

Thermal energy lost to the surroundings Q_{loss} is calculated according to the following formula:

$$Q_{loss} = hS(T - T_{surr}) = hs\Delta T$$

(S2)

where h is the heat transfer coefficient, S is the surface area of the container.

When the temperature reaches the maximum value, the system is in balance.

$$Q_s = Q_{loss} = hS(T_{max} - T_{surr}) = hs\Delta T_{max}$$

(S3)

ΔT_{max} is the average steady-state temperature change. The effective light-to-heat conversion per unit mass lignin η_1 is calculated according to the following formula:

$$\eta_1 = \frac{hS\Delta T_{max}}{m\omega}$$

(S4)

where m is the the mass of compound; ω is the mass fraction of lignin.

The light-to-heat conversion efficiency η_2 for composite is calculated according to the following formula:

$$\eta_2 = \frac{hS\Delta T_{max}}{I}$$

(S5)

where I is the laser power (I=0.32 W).

In order to obtain the hS, a dimensionless driving force temperature, θ is introduced as follows:

$$\theta = \frac{T - T_{surr}}{T_{max} - T_{surr}}$$

(S6)

$$d\theta = \frac{1}{T_{max} - T_{surr}} dT = \frac{1}{\Delta T_{max}} dT$$

(S7)

where T is the temperature of sample in real time, T_{ave} is the maximum steady-state system temperature, and T_{surr} is the initial temperature. Then substituting Eq. S7 into Eq. S1 and rearranging to get:

$$\frac{d\theta}{dt} = \frac{hS}{\sum_i m_i C_{P,i}} \left(\frac{Q_s}{hS\Delta T_{max}} - \frac{\Delta T}{\Delta T_{max}} \right)$$

(S8)

The sample system time constant τ_s:

$$\tau_s = \frac{\sum_i m_i C_{P,i}}{hS}$$

(S9)

So we can get:

$$\frac{d\theta}{dt} = \frac{1}{\tau_s} \frac{Q_s}{hS\Delta T_{max}} - \frac{\theta}{\tau_s}$$

(S10)

when the laser is off, $Q_s = 0$, therefore

$$\frac{d\theta}{dt} = -\frac{\theta}{\tau_s}$$

(S11)

$$t = -\tau_s \ln \theta$$

(S12)

Take t as the y-axis and lnθ as the x-axis to plot, and the cooling time τ_s can be obtained from the slope. Finally get the η_1 and η_2 of the sample.

For the calculation of η_1, all the temperature in formulas are collected from average temperature curve. under the illumination of 808 nm laser light with a power density of 0.78 W/cm^2, wen choose a normal heating and cooling cycle for calculation (Fig. S18c). According to Eq. S12 and Fig. S19c, the cooling time constant of L6Z15 compound was obtained τ_s = 25.249 s. Integral specific heat capacity C_p = 2.04 J (g·°C)$^{-1}$ was obtained from Fig. S16c. The sample mass (m_i) was 0.0152 g and the laser power (I) is 0.32 W, Finally, the effitive

photothermal conversion effiency of P100L6Z15 is calculated to be 16.0 J/g.s.

For the calculation of η_2, all the temperature in formulas are collected from average temperature curve. under the illumination of 808 nm laser light with 0.32 W, wen choose a normal heating and cooling cycle for calculation (Fig. S20b). According to Eq. S12 and Fig. S20d, the cooling time constant of P100L6Z15 compound was obtained τ_s = 41.531 s. Integral specific heat capacity Cp = 2.04 J $(g\cdot°C)^{-1}$ was obtained from Fig. S17c. The sample mass (m_i) was 0.0152 g and the laser power (I) is 0.32 W, Finally, the effitive photothermal conversion effiency of P100L6Z15 is calculated to be 52.9%.

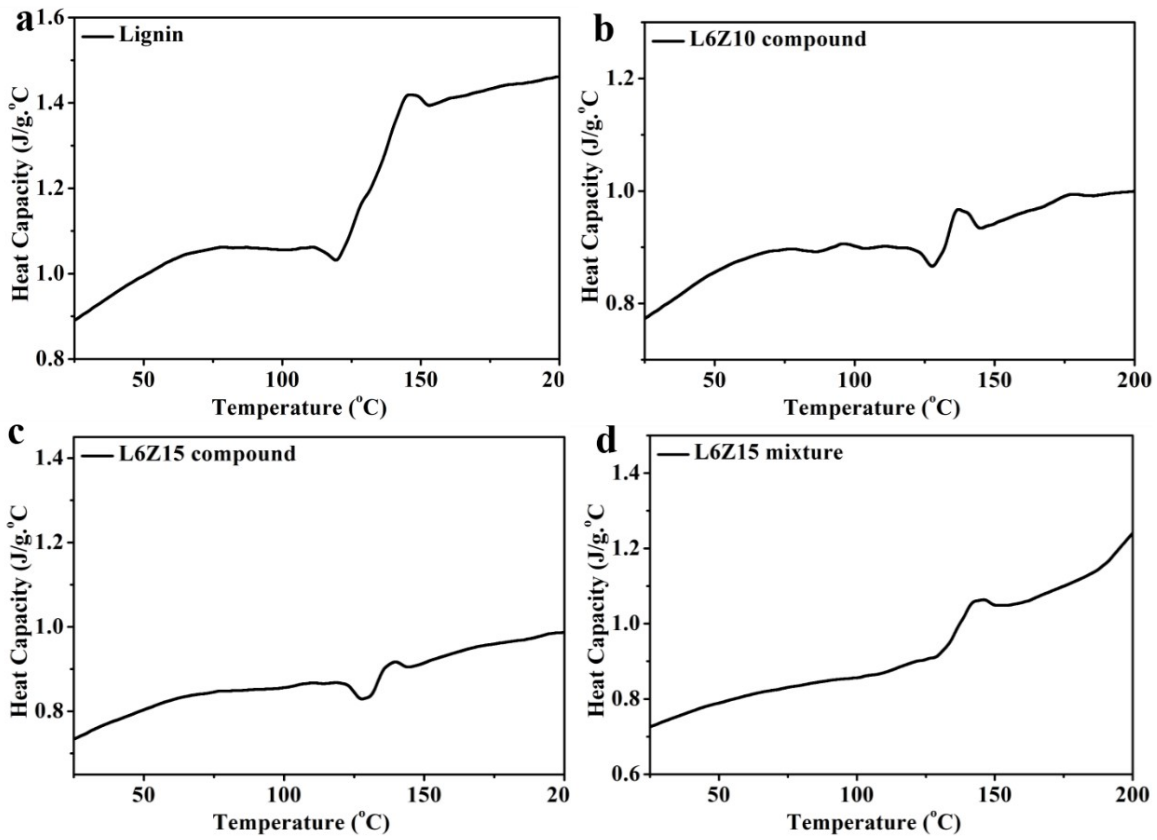

Fig. S16. The specific heat capacity for coordination compounds. The specific heat capacity for **a** lignin, **b** L6Z10 compound, **c** L6Z15 compound and **d** L6Z15' mixture at 25 °C-200 °C

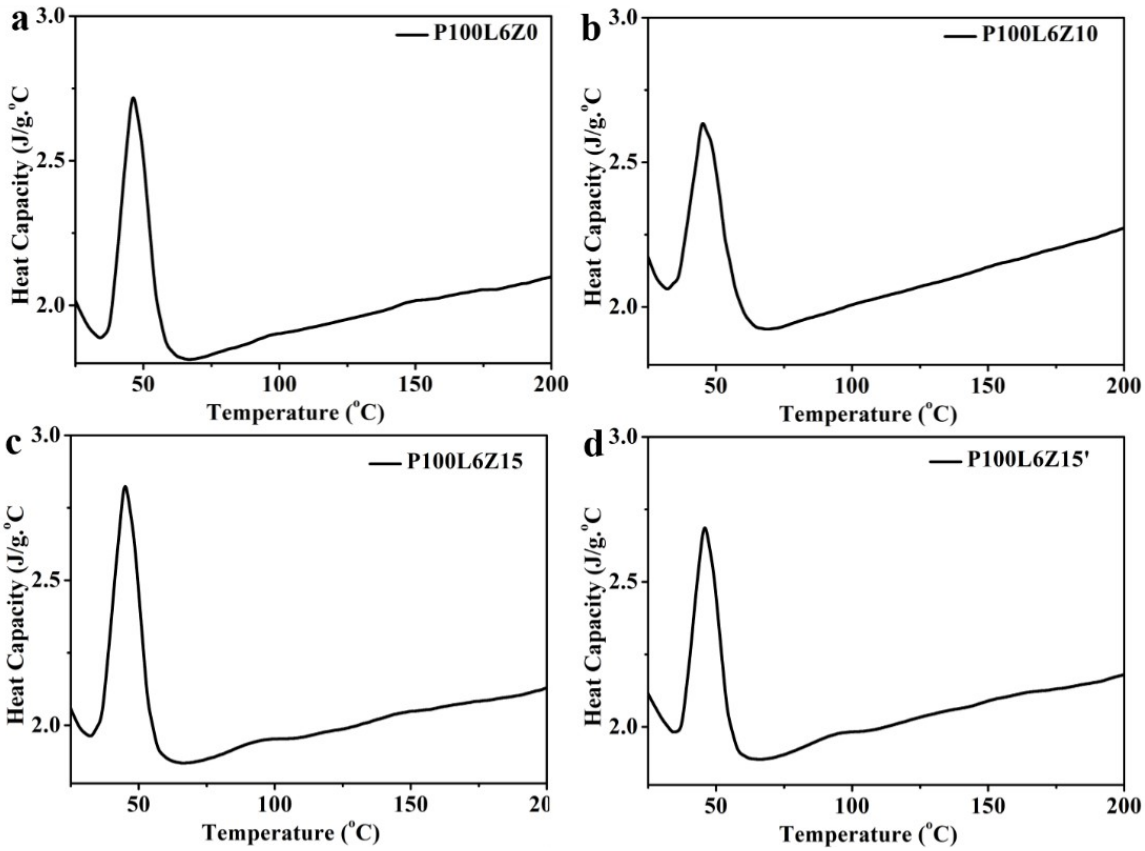

Fig. S17. The specific heat capacity for composites. The specific heat capacity for composites **a** P100L0Z15 without lignin, **b** L6Z0 without ZDMA, **c** P100L6Z15 and **d** P100L6Z15' (directly compounded without ball milling) at 25 °C-200 °C.

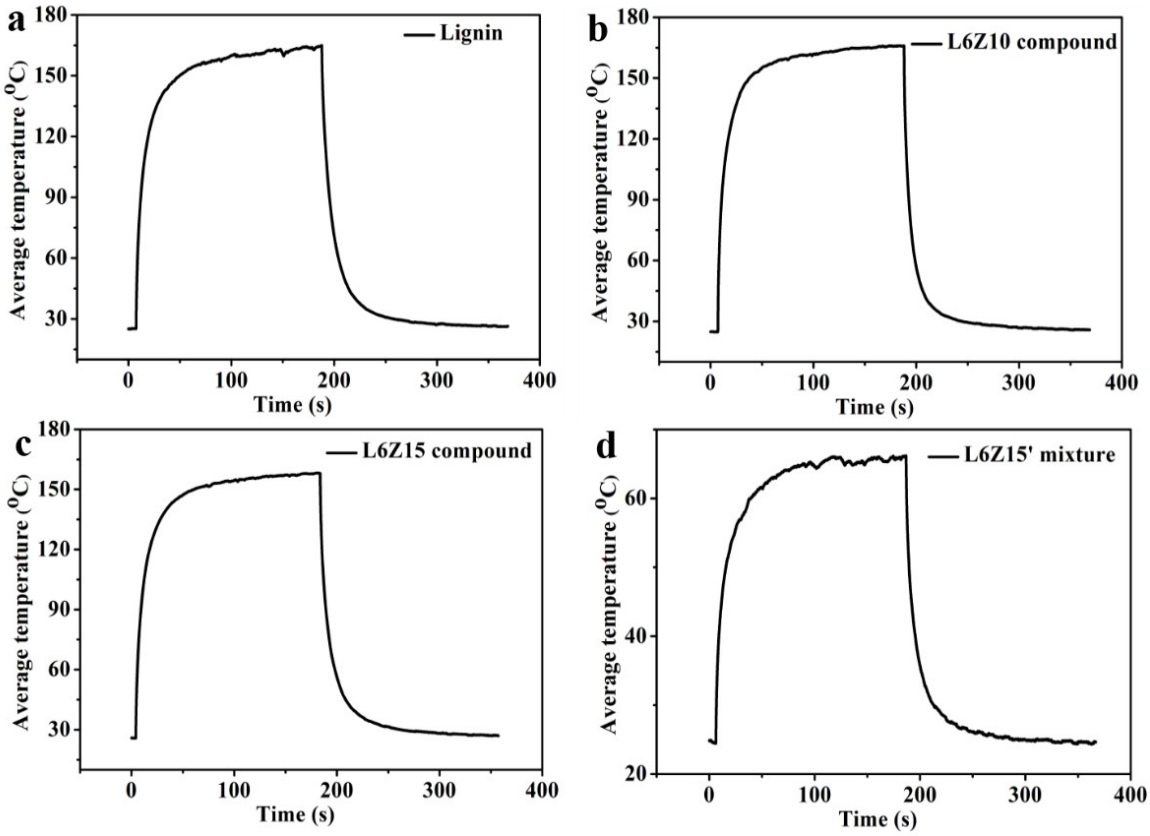

Fig. S18. The average temperature curves for coordination compounds. The surface average temperature variation for **a** Lignin, **b** L6Z10 compound, **c** L6Z15 compound and **d** L6Z15 mixture under the 0.78 W/cm^2 of 808 nm NIR laser.

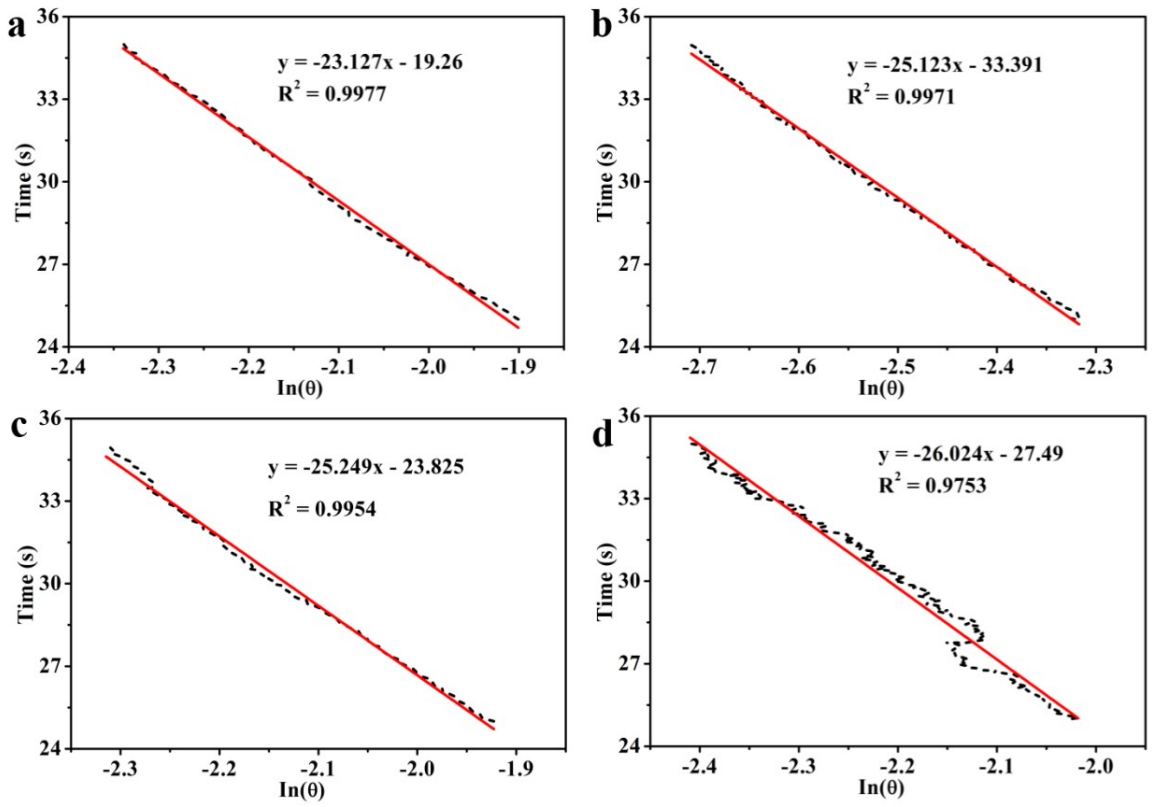

Fig. S19. Time-lnθ linear curve for coordination compounds. The corresponding time-lnθ linear curve of the heating and cooling cycle of **a** Lignin, **b** L6Z10 compound, **c** L6Z15 compound **d** L6Z15 mixture.

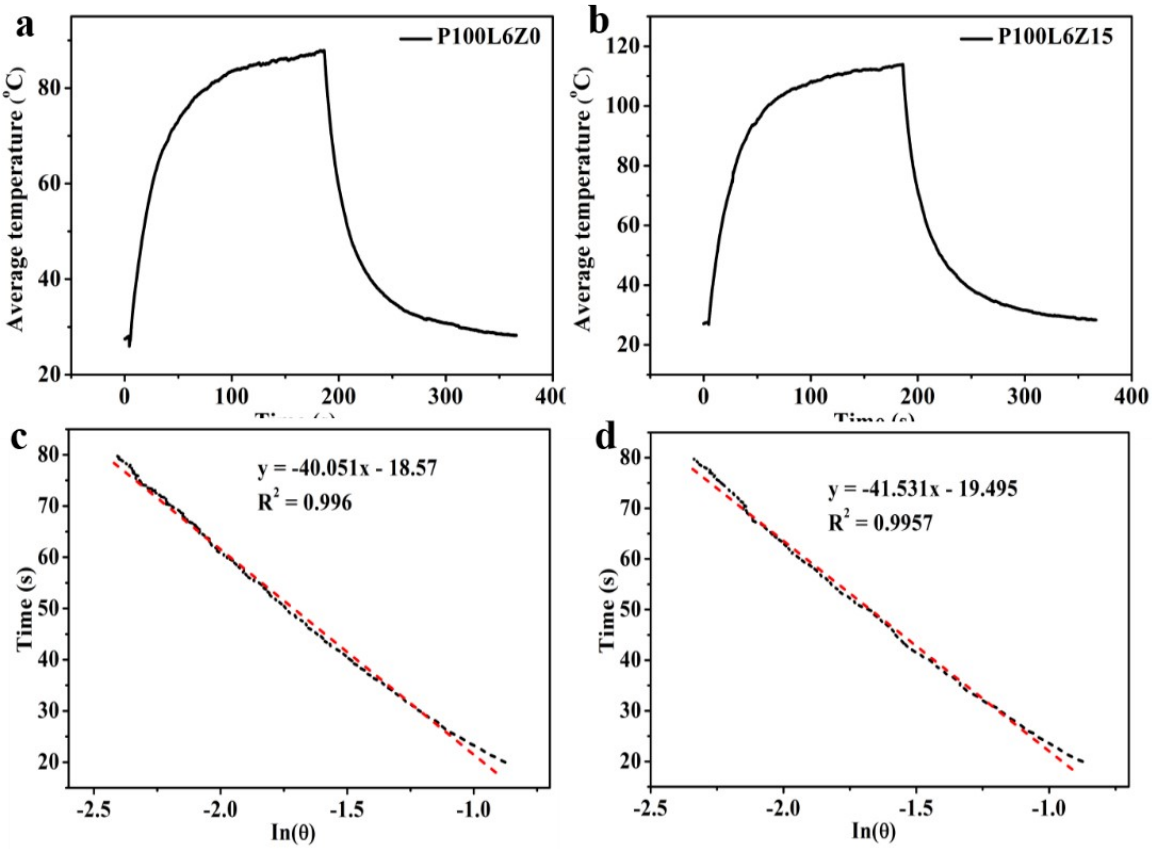

Fig. S20. The average temperature curves and time-lnθ linear curve for composites. The surface average temperature variation for **a** P100L6Z0 and **b** P100L6Z15; The corresponding time-lnθ linear curve of the heating and cooling cycle of **C** P100L6Z0 and **d** P100L6Z15.

Table S1 Summary of related performance of phototropism materials presented in this work comparing with reported literatures.

Materials	Photothermal conversion agent	Temperature response window	Light tracking response time	Light intensity (W/cm^2)
EPDM (this work)	Lignin-based compound	-30-90 °C	2.5 s	1.77
PDMS/silk inverse opal[12]	Gold nanoparticle	---	15 s	0.35
Poly(N-isopropylacrylamide) Hydrogel[13]	Gold nanoparticle; Reduced graphene oxide	20-50 °C	3.5 s	38.22
Poly(N-isopropylacrylamide) Hydrogel[14]	Reduced graphene oxide	27.5-33.0 °C	≈ 75s	---
Liquid crystal elastomer[15]	MXene	55.1-80.8 °C	30 s	1.0
Liquid crystal elastomer[16]	Carbon nanotube	---	≈ 60 s	≈ 0.1
Liquid crystal elastomer[17]	Indocyanine green dye	20-80 °C (heating); 20-40 °C (cooling)	≈ 55 s	---
Azobenzene-containing liquid crystal fiber[18]	---	---	≈30 s	0.075
PAN film[19]	CuS nano-sheet	22.2-40.3 °C	> 600 s	0.1

References

1. Y. Meng, Z. Wei, Y. L. Lu and L. Q. Zhang, *Express Polym. Lett.*, 2012, **6**, 882-894.
2. Gaussian 16, Revision A.03, M. J. Frisch, G. W. Trucks, H. B. Schlegel, G. E. Scuseria, M. A. Robb, J. R. Cheeseman, G. Scalmani, V. Barone, G. A. Petersson, H. Nakatsuji, X. Li, M. Caricato, A. V. Marenich, J. Bloino, B. G. Janesko, R. Gomperts, B. Mennucci, H. P. Hratchian, J. V. Ortiz, A. F. Izmaylov, J. L. Sonnenberg, D. Williams-Young, F. Ding, F. Lipparini, F. Egidi, J. Goings, B. Peng, A. Petrone, T. Henderson, D. Ranasinghe, V. G.

Zakrzewski, J. Gao, N. Rega, G. Zheng, W. Liang, M. Hada, M. Ehara, K. Toyota, R. Fukuda, J. Hasegawa, M. Ishida, T. Nakajima, Y. Honda, O. Kitao, H. Nakai, T. Vreven, K. Throssell, J. A. Montgomery, Jr., J. E. Peralta, F. Ogliaro, M. J. Bearpark, J. J. Heyd, E. N. Brothers, K. N. Kudin, V. N. Staroverov, T. A. Keith, R. Kobayashi, J. Normand, K. Raghavachari, A. P. Rendell, J. C. Burant, S. S. Iyengar, J. Tomasi, M. Cossi, J. M. Millam, M. Klene, C. Adamo, R. Cammi, J. W. Ochterski, R. L. Martin, K. Morokuma, O. Farkas, J. B. Foresman, and D. J. (2016). Fox, Gaussian, Inc., Wallingford CT.

3. J. P. Perdew, K. Burke and M. Ernzerhof, *Phys. Rev. Lett.* 1996, **77**, 3865-3868.
4. J. P. Perdew, K. Burke and Ernzerhof, M. (1997). Errata: Generalized gradient approximation made simple. Phys. Rev. Lett. *78*, 1396.
5. S. Grimme, S. Ehrlich and L. Goerigk, *J. Comp. Chem.*, 2011, **32**, 1456-1465.
6. W. J. Hehre, R. Ditchfield and J. A. Pople, *J. Chem. Phys.*, 1972, **56**, 2257-2261.
7. P. C. Hariharan and J. A. Pople, *Theor. Chim. Acta.*, 1973, **28**, 213-222.
8. A. V. Marenich, C. J. Cramer and D. G. Truhlar, *J. Phys. Chem. B*, 2009, **113**, 6378-6396.
9. Y. Cao, J. Dou, N. Zhao, S. Zhang, Y. Zheng, J. Zhang, J. Wang, J. Pei and Y. Wang, *Chem. Mater.*, 2017, **29**, 718-725.
10. D. K. Roper, W. Ahn and M. Hoepfner, *J. Phys. Chem. C*, 2007, **111**, 3636-3641.
11. Y. Cao, Z. Wang, S. Liao, J. Wang and Y. Wang, *Chem. Eur. J.*, 2016, **22**, 1152-1158.
12. Y. Wang, M. Li, J. K. Chang, D. Aurelio, W. Li, B. J. Kim, J. H. Kim, M. Liscidini, J. A. Rogers and F. G. Omenetto, *Nat. Commun*., 2021, **12**, 1651.
13. X. Qian, Y. Zhao, Y. Alsaid, X. Wang, M. Hua, T. Galy, H. Gopalakrishna, Y. Yang, J. Cui, N. Liu, M. Marszewski, L. Pilon, H. Jiang and X. He, *Nat. Nanotechnol.*, 2019, **14**, 1048-1055.
14. J. Qin, K. Chu, Y. Huang, X. Zhu, J. Hofkens, G. He, I. P. Parkin, F. Lai and T. Liu, *Energy Environ. Sci.*, 2021, **14**, 3931-3937.
15. M. Yang, Y. Xu, X. Zhang, H. K. Bisoyi, P. Xue, Y. Yang, X. Yang, C. Valenzuela, Y. Chen, L. Wang, W. Feng and Q. Li*, Adv. Funct. Mater.*, 2022, DOI: 10.1002/adfm.202201884.
16. C. Li, Y. Liu, X. Huang and H. Jiang, *Adv. Funct. Mater.*, 2012, **22**, 5166-5174.
17. H. Guo, M. O. Saed, and E. M. Terentjev, *Adv. Mater. Technol.*, 2021, **6**, 2100681.
18. L. Liu, M. D. Pozo, F. Mohseninejad, M. G. Debije, D. J. Broer and A. P. H. J. Schenning, *Adv. Optical Mater.*, 2020, **8**, 2000732.
19. Z. Liu, Z. Zhou, N. Wu, R. Zhang, B. Zhu, H. Jin, Y. Zhang, M. Zhu and Z. Chen, *ACS nano*, 2021, **15**, 13007-13018.

Explanation for Videos

Video 1: The light-tracking course for P100L6Z15@600% under the 808 nm NIR laser at 0.95 W/cm^2.

Video 2: The light-tracking course for P100L6Z15@600% under the 808 nm NIR laser at 1.77 W/cm^2.

Video 3: The light-tracking course for P100L6Z15@600% under the stimulation of xenon lamp.

Video 4: The P100L6Z15@600%-assembled solar cells under the stimulation of under the xenon lamp.

Video 5: The P100L6Z15-assembled solar cells under the stimulation of under the xenon lamp.